Frontiers in Neurology and Neuroscience Research
Volume 2
Article ID: 100012
DOI: 10.51956/FNNR.100012

Review Article

Safe MRI of Deep Brain Stimulation Implants: A Review of the Promises and Challenges

Maryam Arianpouya[1,2*], Benson Yang[1], Fred Tam[1], Benjamin Davidson[3,4,5], Clement Hamani[3,4,5], Nir Lipsman[3,4,5] and Simon Graham[1,2]

[1]Physical Sciences Platform, Sunnybrook Research Institute, Canada

[2]Department of Medical Biophysics, University of Toronto, Canada

[3]Harvitz Brain Sciences Program, Sunnybrook Research Institute, Canada

[4]Harquail Centre for Neuromodulation, Sunnybrook Health Sciences Centre, Canada

[5]Department of Medicine, Division of Neurosurgery, Sunnybrook Health Sciences Centre, University of Toronto, Canada

***Corresponding author**: Maryam Arianpouya, Department of Medical Biophysics, University of Toronto, Sunnybrook Health Sciences Centre, S6-Wing, Toronto, ON M4N3M5, Canada; E-mail: maryam.arianpouya@mail.utoronto.ca

Received: April 15, 2021; **Accepted**: May 24, 2021; **Published**: May 31, 2021

Abstract

In the mid-1980s, deep brain stimulation (DBS) was introduced to treat movement disorders. Since then, continuous technological improvements have made DBS an effective treatment for many neurodegenerative diseases, with treatment efficacy critically depending on the precise placement of one or more electrodes in their intended targets deep within the brain. Magnetic resonance imaging (MRI) is highly desirable as a guidance tool in this context, due to its unsurpassed ability to depict the brain with striking soft-tissue contrast. Post-implantation MRI is also desirable to detect possible post-surgical complications (e.g. hemorrhage), and comorbidities of DBS patients in the years after device implantation. However, MRI of DBS patients poses safety risks - primarily the potential for excessive device heating and thermal damage to brain tissue. The heating risk has severely constrained the use of MRI in DBS patients to date. Although some medical centers are exploring "off-label" DBS and MRI applications, many others remain conservative and adopt a "no-MRI" policy for DBS patients.

Extensive MRI physics and engineering efforts have been made to (1) understand the physical interactions of MRI with DBS implants; (2) characterize the safety risks; and (3) provide recommendations and mitigations -yet a robust, safe and general solution for MRI of DBS patients remains elusive. This state of affairs is primarily due to the very complex interactions that can occur between DBS devices and MRI (in all its variations). In this review, the present state of knowledge is reviewed from a historical perspective, discussing the factors leading to these complexities, and looking toward the bioengineering solutions that are emerging in this highly multidisciplinary field.

Keywords: *Deep Brain Stimulation (DBS), Magnetic Resonance Imaging (MRI), MRI-medical device interactions, safety*

Introduction

Deep brain stimulation (DBS) [1] is an established neurosurgical technique to alleviate the symptoms for patients with various brain conditions, when other treatment options fail. DBS therapy was first approved for Essential Tremor (ET) in Europe in 1995, then by the US Food and Drug Administration (FDA) in 1997 [2,3]. The European (CE Mark) approval for treatment of Parkinson's disease was obtained in 1998, and FDA approval followed in 2002 [4-6]. Deep brain stimulation is also approved for the treatment of dystonia [7], and Obsessive Compulsive Disorder (OCD) through the Humanitarian Device Exemption (HDE) process in the US and by CE Mark in Europe [5]. For the treatment of epilepsy, DBS is CE Mark approved in Europe but remains unapproved in the US [5,8]. Research is actively underway to investigate additional clinical applications such as depression [9,10], and eating disorders [11,12].

Globally, ~10,000 patients undergo DBS surgery each year [13]. In 2019, a 32-month-old girl with severe dystonia became the world's youngest patient to receive a DBS implant [14]. To date, DBS has been used for more than 20 different indications and ~40 different brain targets, with more than 175,000 DBS devices (including 170,000 Medtronic implants alone) implanted globally since 1987 [6,13,15-17].

A DBS device consists of four components: (1) a flexible stimulation probe containing wires connected to active metallic electrodes interfacing with the target tissue deep in the brain; (2) a fixation cap fastened to the probe in the skull; (3) a long extension lead, connecting the probe wires to (4) an Implanted Pulse Generator (IPG) which, for practicality, is implanted under the collarbone or in the abdomen [18]. As shown in Figure 1, the DBS leads can be unilateral or bilateral, with either single or dual IPGs.

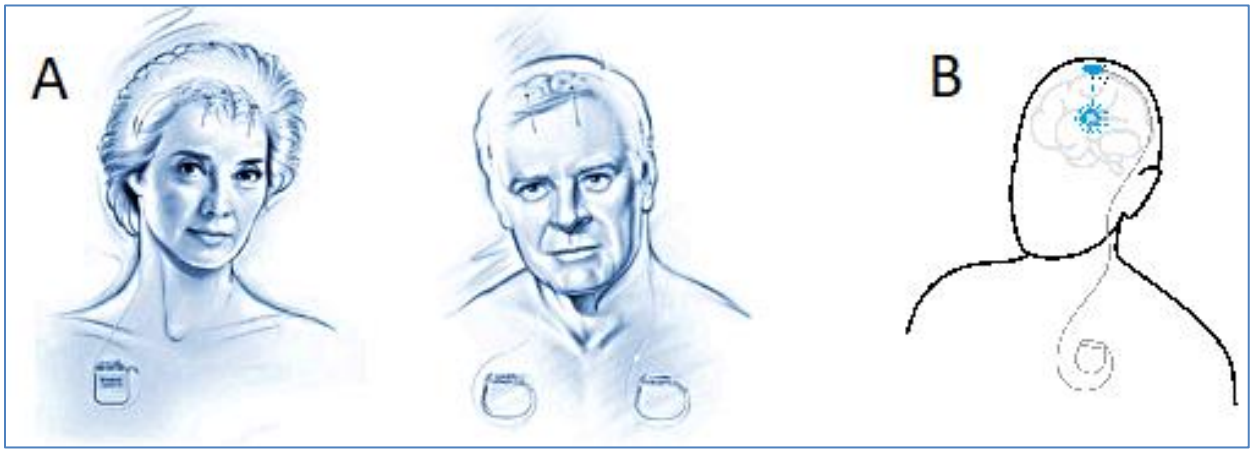

Figure 1. Typical DBS configurations: (**A**) bilateral DBS devices involving two leads and either one IPG (left) or two IPGs (right); (**B**) unilateral DBS device involving one lead and one IPG. Images courtesy of (**A**) Medtronic Inc. (Activa PC or Activa RC, left and Activa SC, right) and (**B**) Abbott (St. Jude Medical Infinity). Images modified from [19].

The implantation procedure varies widely among clinical centers, according to local neurosurgical practice and the technical resources available. Despite the differences, the ultimate goal is to implant the probe as accurately as possible in the target of choice and avoid other neighboring nuclei in the brain. Accurate targeting is critical because: (1) inaccuracy results in high stimulation amplitudes and lower thresholds for stimulation-induced side effects [20]; (2) such side effects, including muscle contractions, gait problems, paresthesia, and ocular deviations can be very problematic [21]; possibly requiring (3) additional surgery to reposition DBS devices, with associated cost, risk, and morbidity [21].

The need to position DBS electrodes very precisely thus places heavy demands on visualizing the desired targets in the brain. Presently, the modality of choice for visualization is Magnetic Resonance Imaging (MRI) due to its ability to depict abnormal and normal neural tissue with excellent signal contrast. Currently, the majority of clinical MRI systems operate at 1.5 Tesla (T) static magnetic field, with 3.0 T systems the second most prevalent [22]. As higher contrast to noise ratio is obtained with MRI at higher fields, increasing focus is being directed to imaging at 3.0 T and even the much rarer systems operating ultra-high fields (7.0 T and above) to enhance localization of the small targets for DBS (Figure 2). However, MRI of DBS patients at 3.0 T and above remains largely aspirational at present. For those DBS devices that can be subjected to MRI under certain conditions (i.e., “MRI-conditional”), imaging has mostly (exceptions noted below) been restricted to 1.5 T with a transmit/receive head coil and a Radiofrequency (RF) power absorption, or Specific Absorption Rate (SAR), of 0.1 W/kg [23-25] due to the risks associated with the MR environment.

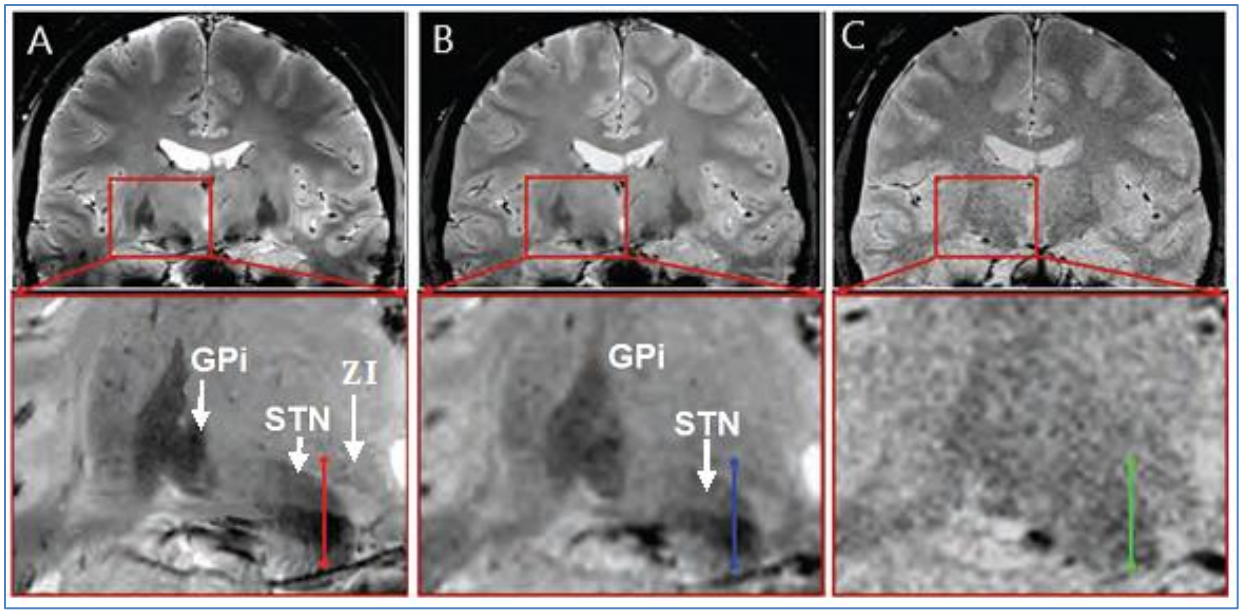

Figure 2. (A) 7 T, (B) 3 T and (C) 1.5 T MRI coronal views of the subthalamic area (top row), and their corresponding magnified views (bottom row) with labeled structures of interest: STN (subthalamic nucleus) and ZI (zona incerta) are favorable targets for PD [26]; the globus pallidus pars interna (GPi) is also a target for PD and some types of dystonia [27,28]. Thalamus subregions are not distinguishable at 1.5 T; increasing magnetic field strength to 3 T and 7 T makes them more visible. The image is adapted from [29].

It might be initially surprising that the primary limit on MRI of patients with DBS implants concerns RF power absorption. In principle, there are at least four different safety risks of MRI-DBS interactions, which occur due to the main electromagnetic components of an MRI system: the large static magnetic field; the use of pulses of RF energy for resonant excitation of magnetization from predominantly water molecules within biological tissues, for imaging purposes; and the use of "imaging gradients" that are pulsed on and off for spatial encoding of magnetization and subsequent image formation. The four safety risks can be arranged in order from 'severe' to 'negligible' as follows [30]:

1. **RF heating** could expose patients to severe risk of transient or permanent neurological dysfunction and hemorrhage, primarily localized to areas surrounding the DBS electrodes
2. **MR artifact** (signal loss or geometric distortion) could impair the ability to evaluate brain tissue adjacent to the leads and electrodes
3. **Induced voltages** could damage IPG circuitry or affect "ON/OFF" modes of operation
4. **Linear or rotational force** could cause tissue damage due to electrode vibration or movement

These known effects of metallic implants in MRI initially caused DBS devices to be labeled by regulatory authorities as 'MR unsafe'. This status was changed for specific DBS devices to 'MR conditional' in 2013, after three decades of research characterizing medical device behaviour in MRI environments led manufacturers to make inroads in device materials and electronics that substantially reduced risks (2)-(4). The risk of RF heating remains problematic, however, as shown in many studies measuring temperatures at the probe tips [31-38] and the IPG housing [39] during MRI. A wide range of heat levels has been reported, from 1°C [31] to as much as 45°C [32], the latter observed at ultrahigh magnetic field. Numerous interacting factors influence the degree of heating [30,40-48]: the type of RF "coil" that is used for resonant excitation (e.g. the standard body or head coils on a given MRI system, or coils purchased from third-party vendors); the patient morphology, anatomical composition and thermoregulatory capacity, and position in the coil; the type of MRI "sequence" used to create images with a specific type of signal contrast; the duration of the sequence; the static magnetic field strength of the MRI system (e.g. 1.5 T or 3 T); the location of the measured temperature; the status of DBS device (e.g. whether 'ON' or 'OFF'); the device design, orientation and trajectory; the

temperature measurement procedure; and the effects of head motion and other physiological fluctuations on the results. Many of these influences are either poorly unrecognized or poorly addressed by existing testing techniques [49], such that the problem of localized RF heating still remains substantial.

Aims

Several articles already provide excellent reviews of medical device safety in the context of MRI [30,42,50], including of (1) physical principles underlying the four major interactions; (2) the relevant regulatory standards concerning implant-related heating in MRI; (3) safety assessment techniques such as computational modeling, numerical simulations and measurement procedures; and (4) mitigation strategies for implant heating including recommendations for the manufacturers. Here we review the present state of knowledge, emphasizing that considerable work remains to create safe conditions where patients with DBS can be imaged using the full capabilities offered by MRI system technology.

Historical Evolution of DBS

The development of DBS from initial discovery to modern capability can be described in terms of four major milestones:

Early stage developments

Electrical stimulation has been applied to treat several neurological diseases since ancient times [51]. Fish known for producing electric discharge were used to treat depression, pain, headache, and seizures prior to the eighteenth century [52,53]. In the 1800s, Aldini electrically stimulated the muscles of animals (and even recently executed criminals), demonstrating the importance of bio-electrical signalling, and leading to his use of transcranial electric stimulation to treat neuropsychiatric disorders [54,55]. These early studies encouraged scientists to "listen" to the signals originating from deep inside the brain; to apply similar electrical impulses to investigate the neurophysiologic functioning of the central nervous system; and to consider electrical stimulation for therapeutic purposes.

Ablation therapy

Irreversible ablative procedures such as pallidotomy were investigated as early as the 1940s, to create permanent lesions in regions of the brain responsible for abnormal electrical signalling and thus provide relief from movement-associated symptoms of disease [56]. To identify the best lesion targets [57], "depth electrography" was developed side-by-side with ablation therapy. Analogous to the recording of cortical potentials by electroencephalography, depth electrography provided essential electrophysiological information about abnormal neural firing patterns in deep subcortical regions of the brain.

Stimulated depth electrography

A technological refinement was developed to the depth electrography method in the early 1950s, enabling stimulation of various subcortical zones using multi-contact electrodes implanted with local anesthesia in the scalp. Following stimulation, electrophysiological responses were recorded from the same electrodes. Patients often lived with the electrodes for weeks [58] to several months [57] to identify the incremental staged lesional sites in the target area [59,60]. Various combinations of electrodes and contacts of electrodes could be inserted, depending on the particular problem and the recording equipment available. Figure 3a shows a total of 36 recording contacts (six 50-micron electrodes incorporating six electrical contacts each), with x-ray images used to evaluate the electrode placement. The contact electrodes were made of copper in early studies, then stainless-steel with the leads (wires) made of platinum alloy later. Copper implants produce toxic reactions in brain tissues leading to neuroinflammatory response at weeks or months after implantation, whereas platinum alloys exhibit good biocompatibility and resistance to corrosion [61,62]. Researchers were intrigued by the effects that were observed in patients during depth stimulation, which

included sensations of bright light, head and eye movements, clinical seizures, confusion, syncopal attacks, vesical sensations and spontaneous laughter, among others (Figure 3b) [57,58].

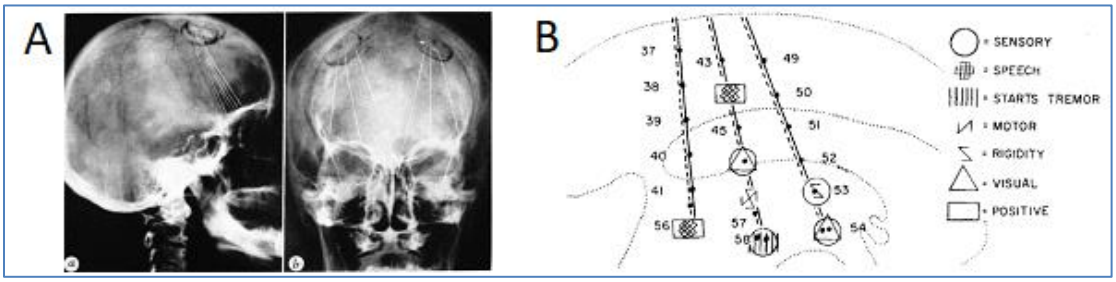

Figure 3. (A) post-implantation X-ray image of depth multi-contact electrodes (1954) [58] and (B) the results of depth electrographic stimulation at various cortical depths in a patient with Parkinson's disease (1965) [57].

Modern DBS therapy

The two main drawbacks of ablation therapy—misplaced lesions, and the irreversibility of ablation—provided impetus for DBS to emerge in the late 1990s as a promising treatment alternative [4]. The modern era of DBS to treat movement disorders began in 1987 when Benabid reported the interruption of Parkinsonian tremors using high frequency (100 Hz) stimulation of the thalamic ventral intermediate nucleus [1]. Numerous studies have confirmed these results using electrical stimulation to thalamic targets, paving the way for the marketing of DBS devices [63]. Medtronic (Minneapolis, MN, USA) received regulatory approval for their first commercial DBS device in 1995, with other companies soon responding and the devices becoming more elaborate over time. For example, Abbot (St. Paul, MN, USA), formerly known as St. Jude Medical, and Boston Scientific (Natick, MA, USA) introduced two new features: (1) segmented electrodes for steering the electric field distribution to deliver new stimulation patterns; and (2) a current-controlled rechargeable IPG for transmitting specific stimulation parameters to each electrode [5,64-66]. Anderson et al. [67] recently showed some examples of FDA-approved DBS leads currently available on the market, as well as new designs under clinical trials or early phase research (Figure 4).

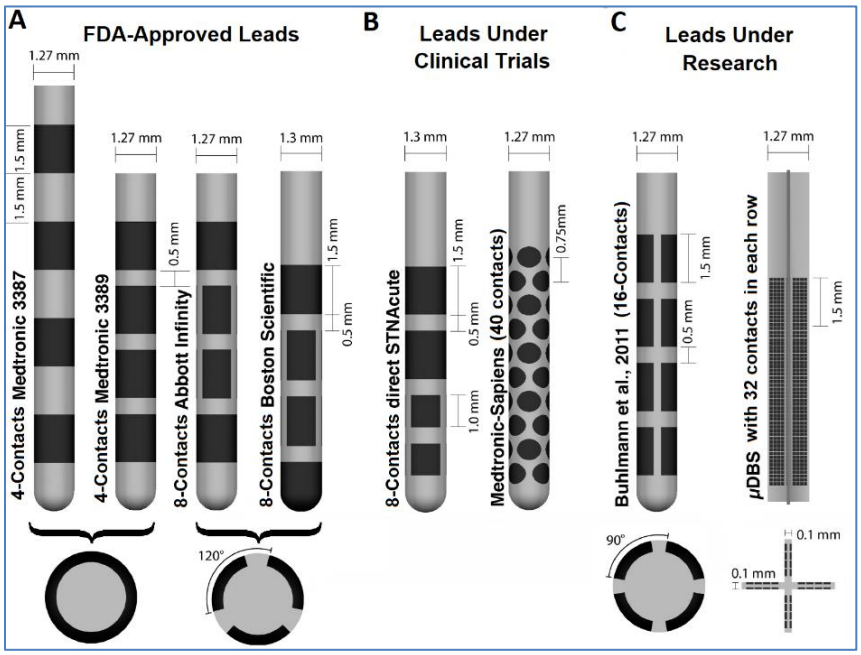

Figure 4. Several DBS Lead devices with different electrode patterns (top) and electrode cross-sections (bottom): (A) FDA-approved Leads from three manufacturers; (B) Leads under clinical trials; and (C) Leads under research, featuring the 16-contact lead design by Buhlmann et al. [68] and the microarray-based DBS lead by Willsie et al. [69]. The image is adopted from [67].

Role of MRI in DBS

The acceptance of DBS as an effective therapeutic intervention has come from several crucial factors [63]: (1) the reversible and adjustable nature of stimulation technique compared to ablative surgery; (2) reproducible, highly effective therapeutic results from numerous clinical trials; (3) readily available DBS devices with flexibility in hardware design and programming; and (4) the parallel growth and adoption of medical imaging modalities, especially MRI which plays a significant and increasing role in the visualization of DBS targets during the surgical procedure and after implantation.

The surgical and imaging protocol is typically implemented in two phases:

Preoperative phase

The target and the associated lead trajectory can be planned stereotactically using standard frames or frameless and standard atlases of the human brain. However, given the wide variability in human brain morphology, brain imaging has the potential to provide better information for surgical planning. At present, 1.5 T or 3.0 T MRI is most desirable for this application but other modalities such as computed tomography (CT) or ventriculography, or some combination thereof may also be applied.

Operative phase

The DBS lead is implanted, followed by the IPG to complete the procedure. The accuracy of lead placement can be validated by several different approaches. A secondary micro- or macro-electrode can be used to record electrical signals created by active neurons at different cortical depths. The recordings are then compared to a registry of characteristic firing patterns of neurons in different brain regions, to provide guidance. Alternatively, intraoperative imaging can be performed after lead placement and before IPG implantation. As this imaging is done in the presence of an implanted device, CT or restricted 1.5 T MRI can be performed. High quality imaging is essential to evaluate any immediate side effects from lead placement that require rapid intervention, e.g. Intracranial Hemorrhage (ICH). The risk for ICH has been reported to be 0.2-5.6%, which can potentially lead to dangerous complications such as paralysis or speech impairment [17,70,71]. Both CT and 1.5 T MRI have low contrast between DBS targets and other brain structures, and typically extend the operative phase so that the patient can be evaluated in a separate medical imaging facility remote from the surgical suite [72]. In practice this can lead to the use of two separate surgical procedures: one to implant the leads, and one to implant the IPG. In some centres, the operative phase is made more efficient by performing lead implantation with “real-time” MRI guidance, in specially designed surgical suites [73-75].

Magnetic resonance imaging also plays an important role in the months and years after DBS devices are implanted. Approximately two-thirds of DBS patients require an MRI exam within 10 years, potentially related to new co-morbid conditions such as cerebrovascular disease – however, only 5% undergo a medically indicated MRI exam [76]. The lack of imaging arises due to factors such as (1) implanted DBS devices that are not MRI-conditional; (2) concerns in many MRI centres about the perceived risks of imaging patients even with MRI-conditional devices [76]; (3) the restricted MRI capabilities and image quality that is achievable with MRI-conditional imaging protocols; and (4) the absence of a complete arsenal of MRI sequences that are available to neurosurgeons for the evaluation of DBS lead placement. For example, MR sequences for low-distortion DBS imaging for targeting of the STN are discussed by Chandran et al. [77], although without considering potential localized heating effects. Separate from clinical needs, there is also an imperative to perform MRI of patients with implanted DBS devices in research trials to improve understanding the DBS mechanism of treatment effect, toward enhancing DBS capabilities. As MRI is highly versatile and can provide spatial information about brain physiological function as well as brain anatomy, certain types of imaging – such as functional MRI of brain activity [78-81], and diffusion weighted imaging of white matter microstructure and tract connectivity [82-84] – have the potential to play an important role in understanding how DBS provides therapeutic

adjustment of regional brain networks to alleviate symptoms, and how inadvertent adjustment of other networks (due to electrode misplacement or insufficiently focal electrical stimulation) leads to side effects. Such sequences may also have an increasing role to play in future clinical practice.

MR Conditional Imaging of DBS Devices

As established by regulatory bodies and evidence provided for certain DBS devices by manufacturers, these devices can be subjected to MRI under certain strict conditions. At present, these conditions primarily involve use of 1.5 T MRI systems with a transmit/receive head coil, pulse sequences with maximum 0.1 W/kg SAR value, and maximum root-mean-square RF transmission amplitude (B_{1rms}) of 2 μT while the DBS device is set to OFF (0V-setting) [23-25]. There are several reasons why these are very limiting constraints.

SAR Restriction

Optimal visualization of DBS target structures typically requires RF power deposition at much higher SAR values than permitted for current regulatory-approved devices. For example, a certain type of MRI pulse sequence known as fast spin-echo inversion recovery (FSE-IR) provides excellent signal contrast between grey and white matter and has been very useful for MRI-guided DBS procedures in Parkinson's disease [85]. However, high-quality FSE exceeds FDA-approved SAR limits and deposits significant heat at the implant tips [47]. The primary cause of heating with FSE sequences is the fast application of a train of RF pulses with high flip angles, which "refocus" magnetization for time-efficient spatial encoding. Work is being conducted to develop FSE alternatives with ultra-low SAR (≤ 0.1 W/kg or 15 times lower than the regulatory limit) using low flip angles, but at present these require approximately double the imaging time [47]. Especially when DBS devices are set to OFF, increasing the imaging time may result in head motion, negatively impacting image quality.

1.5 T MRI Image Quality

As seen in Figure 2, DBS targets are difficult to detect by MRI at 1.5 T whereas higher fields, such as 3 T (and especially 7 T), show clear delineation of the STN, ZI, and GPi. A comparison of STN visualization at 1.5 T and 3 T with T2-weighted FSE imaging for 39 DBS candidates with advanced PD concluded that the STN was visible with a clear margin in all patients at 3 T, whereas it appeared blurred at 1.5 T [86]. In addition, the thalamus is composed of many nuclei [87]. For example, targeting the ventral intermediate nucleus (VIM) of the thalamus has proven effective for DBS treatment of tremors in ET and PD [1]. However, the VIM and other thalamic nuclei are not readily visible with sufficient signal contrast using conventional MRI sequences at 1.5 T and this is posing a challenge even at higher fields [88]. Various MR based techniques have recently been proposed to parcellate the thalamus for direct visualization of the VIM, either requiring use of magnetic fields >3 T [89-91] or high RF power deposition MRI sequences at 1.5 T that exceed imaging safety standards [92-95]. In 2020, Medtronic's Percept PC DBS received FDA approval for 3.0 T full-body MRI, however, restricted to a 0.1 W/kg SAR value, and maximum B_{1rms} of 2.5 μT if the neurostimulator is set to "MRI Mode" [23].

The need for high quality MRI has led to off-label imaging of patients with DBS implants, with some adverse events reported. For example, a serious permanent neurological deficit was reported in 2005, when a DBS patient underwent MRI at 1 T with an IPG [96]. Multiple MRI sequences were performed with SAR ranging from 0.57 to 1.26 W/kg, substantially exceeding the approved limit. However, Boutet et al. [97] performed off-label 3.0 T MRI in 73 patients with active DBS systems, without finding short-term and long-term adverse events. Phillips et al. [98] and Sammartino et al. [99] also conducted 3.0 T-fMRI studies in patients with externalized bilateral DBS electrodes and fully implanted DBS systems (electrodes, extensions, and the IPG) respectively without any transient or permanent adverse events. Zrinzo et al. [100] reviewed over 4000 MRI examinations in patients with implanted DBS hardware reported in the

literature by July 1, 2010. They found 4 adverse events, including 2 hardware failures, 1 temporary and 1 permanent neurological deficit. After this examination, they hypothesized that the probability of MRI-related adverse events is approximately 1 out of 4000. In the same publication, they also mentioned a case report with dyskinesia among 262 MRI examinations including 45 patients with IPGs – a substantially higher rate. Between 2010 to 2012, 4 case reports were published with transient MRI hyperintensities around DBS probes, suggesting significant edema along both electrode tracks [101-104]. The authors speculated on the causes for these effects and were not able to rule out MRI-related mechanisms as the drivers. The various factors affecting DBS-MRI interactions are thus summarized in more detail below.

Factors Affecting DBS-MRI System Interactions

Numerous studies have quantified localized heating effects for DBS devices (or models thereof) during MRI. For example, Georgi et al. [105] found that heating occurring at the electrode tip (15.6°C) might be lower than that found at the phantom surface, in the vicinity where the lead trajectory plunges (59.1°C). Boutet et al. [106] reported a temperature rise of only <2°C at the electrode tips for MRI at 3T using various clinical sequences (such as GRE-EPI = Gradient-Recalled Echo–Echo-Planar Imaging, and 3D SPGR = Three-Dimensional Spoiled Gradient-Recalled Imaging). Bhusal et al. [41] found RF heating fluctuations of 0.1°C to 23.7°C at 1.5 T, and 0.1°C to 7.3°C at 3 T. The variability in these results, and the substantial temperature elevations found in some studies, suggests that the risk of localized heating around DBS electrodes is an important concern – but also that the risk is highly dependent on the nature of the imaging experiment and that there may be factors that have not been applied (or controlled) consistently across this literature. A closer look at these factors is required.

SAR Quantification

The SAR value is defined as the absorbed RF power P_{RF} per exposed total volume of interest (V) (Eq.1), depending on tissue properties ($\sigma(r)$ is the conductivity of tissue at position r, $\rho(r)$ is the density of tissue at r); and MRI system properties (the time averaged E-field magnitude at position r ($|E(r)|^2$) which depends on the type of coil used for RF transmission and the pulse sequence used for imaging):

$$SAR_{volume} = \frac{\langle P_{RF} \rangle_t}{\Delta v} = \frac{1}{V} \int_{volume} \frac{\sigma(r) \cdot |E(r)|^2 dv}{2 \cdot \rho(r)} \quad \rightarrow eq\ (1)$$

When the volume of integration Δv is small, then the SAR value is calculated in a highly position-dependent manner. This is desirable for MRI of DBS devices, as there is potential for a highly localized deposition of RF power in tissues surrounding the lead tip (especially adjacent to the tip and millimetres away). Estimating SAR values with this level of spatial resolution is, unfortunately, not possible on the MRI systems of today. The present ability to measure SAR on clinical MRI systems is limited to an estimate of the average whole-body or whole-head SAR. These estimates are made via sensors in the MRI system, for example to quantify the power transmitted to the patient by measuring the power delivered to the MRI transmitter coil, the power dissipated by the coil, and then subtracting these quantities. The delivered power can then be used in models, calibrated and validated (for example, based on MRI of large animals with invasive temperature probes) such that head-averaged and body-averaged SAR are reasonably well estimated for a given MRI sequence when certain information is entered into the MRI system console, including the mass of the patient [84,107]. These modelling approaches depend on the MRI system manufacturer and are refined over time, such that sites with the same MRI system but different software revision or hardware upgrades may also yield different SAR estimates [108]. These revisions occur in part because MRI system manufacturers are incentivized to ensure that SAR is not overestimated, as improved estimates ultimately enable more RF power to be deposited in patients within regulatory guidelines, enhancing image quality and other MRI sequence capabilities. This situation has introduced uncertainty about how reliably SAR estimates can be used as a standardized measure when considering localized

heating during MRI of DBS devices. For example, one study investigated MRI of a DBS phantom at 1.5 T using two different generation systems from the same manufacturer, observing markedly different SAR estimates and heating effects between the two sets of measurements [109]. This concern has led to some investigation of alternative metrics of transmitted RF power that can be measured more reliably on MRI systems, such as the B_{1rms} value. Although this quantity can be quantified quite accurately by certain MRI sequences, its relationship with the E-field and tissue heating still requires considerable investigation.

Re-stated, the current procedures for estimating SAR on clinical MRI systems do not provide spatially-dependent SAR values. The actual "SAR maps" of RF power deposition during MRI of DBS patients depend on numerous parameters, including patient anatomy and spatially-dependent electromagnetic properties, static posture in the magnet bore and imaging landmark, magnetic field strength, RF transmitter coil and implant materials and lead trajectory. These dependencies can be investigated through electromagnetic modelling and simulation, and numerous simulation studies exist in the literature [110-113]. Direct calculations involving the solution of Maxwell's equations are time-consuming and computationally intensive, and although rapid solvers are being developed [114-116], simulations have yet to become integrated in clinical workflow for DBS patients. It is possible that this could happen in the future, with pre-implant MRI and post-implant CT data used to prime the simulations.

Temperature Quantification

Even if SAR mapping were to become integrated into clinical workflows, the maps would provide only an indirect estimate of the damage that can arise to biological tissues due to RF power deposition. The temperature increase produced by RF power deposition is much more directly relevant. If the local temperature reaches the low 40's (in Celsius) or greater, then thermal damage begins to accumulate in cells as proteins begin to denature. This time-dependent damage process, known as thermal coagulation and thermal necrosis, is usually approximated by an Arrhenius equation [117]. The equation leads to the concept of "thermal dose" and a quantity known as "t_{43}", the equivalent time that tissue would spend at 43°C to accumulate the same level of thermal damage obtained by heating at a given temperature and time duration. The exponential nature of the Arrhenius equation means that in practice, temperatures exceeding approximately 50°C cause thermal coagulation in a few seconds. In neural tissues, the t_{43} values for thermal coagulation are in the range of 0-20 minutes [118], suggesting that even modest temperature elevations may have negative consequences over the timescale of a typical MRI exam. Sublethal effects such as disruptions in nerve conduction, metabolism or neurotransmitter function have been reported in various animal and *in vitro* studies at lower t_{43} values [119]. Thus, there is a significant body of thermal biophysics literature suggesting that permanent or transient thermal effects are of possible concern during MRI of patients with DBS implants.

Multiple MRI parameters are sensitive to temperature and certain forms of thermal therapy, such as high intensity focused ultrasound ablation treatments that provide an alternative to DBS, rely on MRI thermometry approaches to guide thermal dose delivery [120]. In principle, MRI thermometry can be used to map RF power deposition, but there is poor sensitivity to detect small temperature changes and methods have yet to be developed that intersperse thermometry that is sufficiently sensitive into the clinical workflow of MRI sequences. Alternatively, it is possible to simulate temperature elevations if the spatial pattern of SAR values is known. This is typically achieved using the Pennes Bioheat equation [121] although other approaches also exist [122]. The former equation is given by:

$$\rho c \frac{\partial T}{\partial t} - \nabla \cdot k \nabla T - Q_{met} + \rho_b c_b w (T - T_b) = (SAR)\rho \quad \longrightarrow eq\ ②$$

where T is the temperature rise, c is the specific heat capacity, k is the thermal conductivity, Q_{met} is metabolic heating, ρ_b is the mass density of blood, c_b is specific heat capacity of blood, w is the perfusion of blood, T_b is the blood temperature and SAR is the local specific absorption rate. In addition to the fact that all parameters in Eq. 1 and Eq. 2

are position-dependent, the temperature rise is affected by two other major factors: (1) different body compositions will affect power deposition – for example effects of subcutaneous fat in the scalp [41], skull thickness [123], size of ventricles [48] and volumetric fraction of cerebrospinal fluid (CSF) [124] may have an impact; and (2) the electromagnetic properties of the tissues with respect to the RF wavelength influence the SAR level [125-128]. For example, if the tissue dimension is larger than the incident RF wavelength (which decreases as a function of the applied static magnetic field), RF energy absorption occurs predominantly near the patient surface. The highest RF absorption occurs when the tissue is approximately half the size of the incident wavelength [125-128]. These factors have increasingly led some investigators to propose the use of realistic "anthropomorphic" phantom test objects to evaluate localized heating effects during MRI of DBS devices [129].

Thermoregulation

The parameters Q_{met} and w in Eq. 3 call attention to the thermoregulatory capabilities of the brain. Specifically, the brain is normally able to dissipate low to modest levels of RF power deposition (i.e., near regulatory limits) such that the rate of temperature increase is curbed. According to Collins et al. [123], for example, inducing a head average SAR level of 3.0 W/kg is unlikely to produce a significant elevation of core temperature in the brain due to its high rate of perfusion (although this might not be the case for local SAR in any 1g of tissue in the head).

As endotherms, humans maintain a near-constant core body temperature of 36–37.5°C, through homeostatic mechanisms that optimize metabolism [130]. For the deep brain, the average temperature exceeds the core body temperature by slightly less than 1°C, with temperature gradients existing between the cooler cortical regions and warmer basal regions [131]. This highly controlled core temperature is regulated by the hypothalamus and continuously fluctuates due to diurnal, internal, as well as external factors. In the presence of an external thermal challenge of RF radiation, the thermoregulatory system maintains the body temperature via losing heat through multiple mechanisms, including thermal conduction and perfusion [127]. If the thermoregulatory system is unable to thoroughly dissipate the loaded heat, local and/or overall temperature rise occurs in the tissue for a period of time [127]. As explained above, a thermal dose is thus delivered which may have transient or permanent bioeffects. The literature shows that the thermal dose threshold (critical t_{43} value) for bioeffects and thermal coagulation is not well-determined, and thermoregulation is likely a major confound in the existing data. Thermoregulatory processes require more study, although ultimately such work would be most informative if performed in humans – which is difficult to do safely. Furthermore, the capacity for thermoregulation is modulated by other biological factors. For example, Kim et al. [37] investigated a cohort of 69 individuals showing that compared to young patients, older patients experienced about twice the increase in temperature (1°C *vs*. 0.5°C, measured in the ear) after undergoing 3 T MRI of the head. This effect is consistent with age-related decreases in cerebral perfusion and thus decreased ability to dissipate RF power deposition [132].

DBS device aspects

Turning now to the DBS device parameters that affect localized RF heating during MRI, several factors warrant discussion, including: the overall probe length (the lead with the extension); the thickness of the insulation sheath; the lead trajectory (shape) and area of tissue affected; position with respect to the RF transmission coil; and whether implants are unilateral or bilateral [129]. The lead and the extension lengths are predetermined by the manufacturer and range between 10–50 cm and 10–110 cm, respectively. The lengths differ among manufacturers and models, enabling clinicians to choose the appropriate device based on the anatomy and the size of patients, IPG implantation site (chest or abdomen), as well as age (especially considering the high growth rate in children [133]). Because the lead length is typically not a perfect fit, the excess length is kept around the cranium rather than placed against the soft tissue in the neck. Consequently, the configuration of the lead trajectory and the extent of tissue potentially affected by the implant can significantly vary from patient to patient [46].

In 2008, Mattei et al. [48] investigated the complexity of heating effects at the tips of metallic pacemaker leads for cardiac MRI applications at 1.5 T using an RF birdcage coil. Leads of different lengths, shapes, areas of coverage, and thicknesses were implanted in various positions with respect to the edge of a phantom (either box or torso-shaped) and the RF coil. Fibre-optic temperature probes were also included to record temperature elevations at the exposed lead tip. Numerous noteworthy effects were observed that are relevant in the context of DBS. First, significant heating occurred when leads were placed closer to the edge of the phantom or the RF coil. This occurred since the E-field was highest at the edges of the phantom nearest the inner wall of the RF coil. Second, more heating was observed when the leads were placed closer to the location of tuning capacitors on the coil rungs of the birdcage coil, as the capacitors intensified the E-field. Third, the temperature increases were not always proportional to the area covered by the lead, and dependent more on whether the lead trajectory included zones of elevated E-field (i.e. near the phantom surface or capacitor locations). Fourth, for straight leads, heating was highly dependent on lead length, with 25 cm leads producing much more heating than 15 cm or 40 cm leads. This observation agrees with the known "resonant length_ l_{res}" characteristics that occur with straight wire implants which are approximately half the wavelength of the RF transmission (λ_{RFT}) in biological tissue [134]:

$$l_{res} = 0.41\lambda_{RFT} = \frac{1}{2.Re(f\sqrt{\mu\varepsilon_{eff}})} \quad \longrightarrow eq\ ③$$

where f is the operating frequency of MRI (64 MHz for 1.5 T and 128 MHz for 3.0 T); μ is the permeability and ε_{eff} is the effective permittivity of the medium. Under the ASTM phantom condition, the resonant length for 64 MHz is close to 22 cm and 12 cm for 128 MHz (3.0 T) [135]. Fifth, heating was most pronounced when the phantom was placed at the coil isocentre; when the phantom was displaced longitudinally, heating effects were lessened due to accompanying decrease in E-field experienced with closer proximity to the radial end-ring of the coil. Sixth, the dependence of localized heating on thickness of lead insulation was complex, with bare wires showing either less or more heating than insulated wires for realistic lead trajectories and short straight wires, respectively. This suggests that the insulation has an important impact on the extent of RF coupling between the transmitter coil and the implanted device. Seventh, the temperature increase measured inside the human-shaped phantom was about 6°C lower than in the rectangular trunk simulator, emphasizing the need for additional research involving anthropomorphic phantoms, over phantoms with simple geometries.

Two factors not addressed by Mattei et al. [48] were the body composition and the choice of RF transmitter coil on localized heating. The presence of subcutaneous fat in the scalp affects the RF absorption as discussed before. Bhusal et al. [41] examined the effect of body composition on the RF heating by adding an oil layer on top of a 3D-printed human head-shaped saline-filled phantom representing subcutaneous fat. They found that cases with added oil layers had a rise in temperature of 8.8°C at 1.5 T and 4.1°C at 3 T. In addition, the typical case for MRI-conditional devices has been that imaging is permitted using a transmit-receive birdcage head coil, rather than the much larger body transmit coil that encloses the magnet bore [23-25]. This stipulation ensures that the E-field of concern is limited primarily to the head and does not encompass the IPG. Whereas the initial data suggested a safety benefit, the use of a transmit-receive birdcage coil is significantly limiting, in two major respects. First, the signal-to-noise ratio (SNR) of brain images is enhanced by using the body transmit coil together with multi-channel head receiver coils, that are standard components of clinical MRI systems [136]. Second, this SNR increase can be traded for accelerated "parallel imaging" reconstructions that make use of the localized sensitivity profiles of the individual receiver coil elements - typically providing high quality images in half the time or less [137,138]. The potential MRI advantages of using the RF body coil over transmit-receive birdcage head coils have prompted investigators to perform studies that compare the localized heating effects obtained with both transmitters. For example, Kahan et al. showed that switching from head

to body coil increased the temperature at the electrode tip of Medtronic ActivaPC devices at 1.5 T, but that the increase for their specific imaging protocol did not exceed the maximum allowed under safety regulations [45]. These investigators also observed heating effects that exceeded the maximum allowed temperature elevation for their 3 T MRI protocol, prompting them to avoid imaging at this field strength [45].

Electromagnetic simulation studies have also been performed that support and extend such work. For example, Golestanirad et al. [46] simulated the SAR levels and localized temperature increases for MRI at 3.0 T of different bilateral DBS lead trajectories estimated from patient CT data. They showed that localized SAR and temperature increases were substantially elevated for the lead contralateral to the IPG. This led to a new strategy for DBS lead management, which was subsequently verified in phantom experiments: specifically, increasing the number of DBS lead loops around the burr hole significantly reduced the amplitude of localized heating in a linear fashion [41,139,140]. The benefits of such lead management practices need to be demonstrated in replication studies, but the initial results promise significant potential to increase MRI safety for future DBS patients.

When the IPG is connected, and subsequently when the implant is active, additional safety factors must be considered during MRI. First, time-dependent changes in magnetic flux density passing through the cross-sectional area of a conducting material can induce an electric voltage, according to Faraday's law [141]. Both the time-varying imaging gradients and RF magnetic fields can induce such voltages, although the RF transmission field is the much stronger source. Situations where the induced voltages can occur in DBS leads are thoroughly discussed in the literature [30,50]. The induction of voltages and the resulting eddy currents may flow in either direction along the DBS lead, potentially impacting the IPG or the axons surrounding the electrode. Whether the induced current can generate an action potential causing unintentional electrical stimulation of the neural tissue is difficult to determine due various uncertainties. The activation threshold, for example, largely varies according to the number, size, type, and orientation of axons with respect to the induced electric field, as well as the electric properties of the tissue surrounding the electrode [142,143]. The geometry of the electrode and the stimulation parameters could also contribute to potential activation. Irrespective of the precise mechanisms, anecdotal effects have been reported. For example, Davidson et al. [144] recently conducted a phantom study to establish the safety of their 3 T MRI protocol and subsequently performed imaging of six patient volunteers with their DBS in an activated state without any serious adverse events. However, one patient experienced stimulation-related side effects (rhythmic vertigo) during T1-weighted Magnetization-Prepared Rapid Gradient Echo (MPRAGE) imaging with the DBS in an ON state, because of RF modulation of voltage amplitude. The authors hypothesized that the large-amplitude RF pulses during this imaging sequence were constructively interfering to impact the oculomotor nucleus/nerve nearby the DBS target, and subsequently opted in the future to turn DBS devices to OFF for this portion of their imaging protocol.

In addition, various DBS electrode designs are commercially available with new options being introduced into the market (Figure 4). The electrodes are designed with different geometric characteristics, usually with the aim of improving control and localization of the E-field distribution to the intended brain target, while minimizing stimulation of surrounding regions to minimize side effects. Consequently, the device mode is programmed based on the electric field distribution between contacts as the anode or cathode (for bipolar), or contacts as the cathode and the IPG case as the anode (monopolar). In the MRI environment, when the implant is "ON", the RF transmission could potentially modify the E-field for DBS by coupling and grouping the non-active contacts forcing a unique potential for all, altering the operating mode and the stimulation parameters, and potentially causing device malfunction. Additional research is still required to investigate the importance of electrode interaction effects in detail.

Efforts to Reduce MRI-DBS Device Interactions

Several strategies have been investigated to reduce how MRI procedures interact with DBS devices. The two major categories of approach focus on (1) improved MRI methodology and (2) improved device design and manufacturing. The former category has been reviewed recently [42] and includes suppression of RF-related heating using the Parallel Transmission (PTx) technique [111,129,145-151], and the linear-polarization mode of the birdcage RF coil [152,153]. The latter category is reviewed below.

Reducing susceptibility artifact

Typically, during MRI, the static magnetic field becomes spatially inhomogeneous in the vicinity of the DBS lead and electrode. The electrically conductive components of DBS (the Lead and extension wires) are made from Platinum/Iridium (Pt-Ir) alloy and the IPG case is made from Titanium insulated with a thin biocompatible polymeric film. The inhomogeneity arises because of the mismatch in magnetic susceptibility primarily between the metallic device components and the surrounding biological tissue, such that the inhomogeneity represents the transition zone between the different static magnetic fields in the two regions [154]. The inhomogeneity produces characteristic "susceptibility artifacts" in MR images near DBS devices [155], including (1) signal loss due to significant dephasing of the MR signal arising from the "T2*" mechanism; and (2) geometric distortion with focal areas of signal loss or "pile-up" resulting from assignment of MRI signals to the wrong spatial location. The precise appearance of the artifact depends on the amount of susceptibility difference (i.e., DBS device materials), size, shape, and orientation of the lead with respect to the static magnetic field, field strength, and MRI sequence acquisition parameters such as echo time (TE) as well as readout gradient strength and orientation, and readout bandwidth. For example, Pollo et al. [156] imaged the Medtronic Activa 3389 DBS electrode "in passive mode" in a phantom and in 10 patients, measuring the extent of the artifact in three dimensions over the distal contact. It was shown that each contact induced an ellipsoid-shaped artifact, extending symmetrically 1.4 mm over both proximal and distal limits, and 1.16 mm over the lateral limit of the contact.

To minimize susceptibility artifacts, electrode materials have been introduced with magnetic susceptibility that more closely matches that of brain tissue: examples include poly(3,4-ethylenedioxythiophene) (PEDOT), graphene fibre (GF) and semiconductor electrodes. The PEDOT conducting polymers are reliable for neural recording and stimulation electrodes, providing satisfactory electrochemical stability, non-cytotoxicity, and high electrical conductivity. Faradaic (charge transfer) and capacitive (charge redistribution) processes at the PEDOT–tissue interface provide excellent charge-injection-capacity (CIC) [157]. However, PEDOT is used as a coating on electrodes, which still results in some magnetic susceptibility mismatch; and polymer degradation, poor adhesion to metal substrates, and cracking presently make the coating impractical for stable chronic stimulation [158,159]. Alternatively, GF electrodes maintain substantial stability but with slightly lower CIC than that of PEDOT. In 2020, Zhao et al. [155] developed a novel GF DBS microelectrode with little-to-no MRI artifact at 9.4 T. The microelectrodes were reported to have 70 times more CIC than clinical alternatives with Pt-Ir electrodes [155]. Semiconductor electrodes have also been reported with high thermal conductivity and good magnetic susceptibility matching with brain tissue [160]. Beygi et al. [161] developed silicon carbide semiconductor microelectrodes with little-to-no image susceptibility artifacts observed with 7.0T-MRI and conducted simulations that predicted a ~30% reduction in SAR values compared to electrodes made from platinum. Other materials have also been investigated, such as nanocarbon-based ink electrodes printed on organic polymer substrates [162], titanium-based microelectrodes [163], and carbon nanotube (CNT) yarn electrodes [164]. Although these materials are MRI-compatible, they have yet to progress along the commercialization pathway to full clinically approved DBS devices.

Suppression of induced voltages and localized heating

Several implant device designs have been proposed to avoid or minimize the induced voltages, currents and subsequent heating that can potentially occur during MRI. Among the most common methods for this purpose is the "RF shield trap", which consists of dual-conductor structure, analogous to coaxial cables. The inner- and outer-conductors are connected by capacitors that are tuned to resonate with the MRI Larmor frequency. Without making physical contact with any conductor passing through (i.e., in floating position), the shield trap acts as series impedance to the inside conductor. The floating cable trap was initially introduced by Seeber et al. [165] to suppress induced shield currents on surface coil receiver cables. Griffin et al. [166] further developed and miniaturized traps to enhance RF safety during interventional cardiac MRI procedures involving catheters and guidewires, reporting a 40 % reduction in heating compared to guidewires without the trap in place. Subsequently, Alipour et al. [167] improved the design of the shielding wire trap with loose solenoidal windings instead of rigid conducting cylinders, such that 15 min. of 1.5 T MRI with high-SAR sequences (e.g. 4 W/Kg) only increased the temperature at the catheter by 0.7°C, whereas an increase of 5.7°C was obtained without the trap in place.

Another alternative involves manipulating the electrical resistivity of DBS leads, as this quantity substantially influences the SAR value obtained during MRI. Very low resistivity can increase the induced current during imaging, whereas very high resistivity requires the IPG to generate a higher voltage for the same level of stimulating current, which shortens battery life while also posing a potential safety issue [21,168]. Angelone et al. [113] found that resistivity values ρ_{lead} within the range of 0.001 Ωm to 1 Ωm can minimize the dissipation power and generated SAR. Bonmassar et al. [169] proposed a new type of lead that has high resistivity in the RF range, but low resistivity at the much lower frequencies used in DBS. The use of "RF chokes", an inductance coil of very small resistance, also reduces localized heating by creating a high impedance to unwanted currents [170]. Electrically conductive non-metal fibers can also be used to achieve desired resistivity values [171].

Conclusion

Together, the complexities and uncertainties of DBS-MRI system interactions, as discussed in this review, suggest a need for caution and additional MRI safety research. To summarize, (1) multiple patient parameters such as the anatomical geometry and tissue composition influence RF absorption; (2) patient thermoregulatory capabilities vary due to biological factors such as age; (3) RF heating is highly sensitive to multiple lead geometrical and orientational factors, as well as MRI software and hardware factors; (4) ability to measure local SAR and temperature remains limited on clinical MRI systems; and (5) DBS device setting parameters and hardware configurations affect coupling of the device with the MR environment.

To date, most of the heating assessments of MRI-DBS have been restricted to simulations and experiments using phantom test objects. Both approaches are approximations to the actual conditions encountered in clinical trials. In addition, case reports of suspected adverse events because of DBS interactions with MRI have not identified all the probable unsafe settings leading to injuries; nor have all the off-label studies in humans identified all the safe conditions – just the specific protocols that were implemented on certain MRI system hardware and software. More work is required to improve this state of affairs; options include the development of careful experiments in large animal models with invasive thermometry, and continued efforts to improve the realism of simulation and phantom models.

If such work is undertaken, then the potential benefits are important for DBS patients. Safe MRI of these individuals – using more of the full potential of this imaging modality—will help to manage surgical side-effects, evaluate co-morbid disease, and facilitate neuroimaging research to promote enhanced DBS technology.

Acknowledgments

The authors would like to acknowledge the Canadian Foundation for Innovation, the Natural Sciences and Engineering Research Council of Canada and the Canadian Institutes of Health Research for funding this work.

References

1. Benabid AL, Pollak P, Louveau A, Henry S, de Rougemont J (1987) Combined (thalamotomy and stimulation) stereotactic surgery of the VIM thalamic nucleus for bilateral Parkinson disease. Appl Neurophysiol 50: 344-346.
2. Miocinovic S, Somayajula S, Chitnis S, Vitek J L (2013) History, applications, and mechanisms of deep brain stimulation. JAMA Neurol 70: 163-171.
3. U.S. Food & Drug. (2015, November 2017). FDA News Release - FDA approves brain implant to help reduce Parkinson's disease and essential tremor symptoms.
4. Bronstein J M, Tagliati M, Alterman R L, Lozano A M, Volkmann J, et al. (2011) Deep brain stimulation for Parkinson disease: an expert consensus and review of key issues. Arch Neurol 68(2): 165.
5. Sarem-Aslani A, Mullett K (2011) Industrial perspective on deep brain stimulation: history, current state, and future developments. Front Integr Neurosci 5: 46.
6. Medtronic DBS therapy for parkinson's disease.
7. Coubes P, Cif L, El Fertit H, Hemm S, Vayssiere N, et al. (2004) Electrical stimulation of the globus pallidus internus in patients with primary generalized dystonia: long-term results. J Neurosurg 101: 189-194.
8. Bergey GK, Morrell MJ, Mizrahi EM, Goldman A, Stephens DK, et al. (2015) Long-term treatment with responsive brain stimulation in adults with refractory partial seizures. Neurology 84: 810-817.
9. Holtzheimer PE, Mayberg HS (2012) Neuromodulation for treatment-resistant depression. F1000 Med Rep 4: 22.
10. Mallet L, Polosan M, Jaafari N, Baup N, Welter ML, et al. (2008) Subthalamic nucleus stimulation in severe obsessive-compulsive disorder. N Engl J Med 359: 2121-2134.
11. Park RJ, Singh I, Pike AC, Tan JOA (2017) Deep Brain Stimulation in Anorexia Nervosa: Hope for the Hopeless or Exploitation of the Vulnerable? The Oxford Neuroethics Gold Standard Framework. Front Psychiatry 8: 44.
12. Blomstedt P, Naesström M, Bodlund O (2017) Deep brain stimulation in the bed nucleus of the stria terminalis and medial forebrain bundle in a patient with major depressive disorder and anorexia nervosa. Clin Case Rep 5: 679-684.
13. Christen M, Muller S (2012) Current status and future challenges of deep brain stimulation in Switzerland. Swiss Med Wkly 142: w13570.
14. The boss magazine (2019) Youngest Recipient of Deep Brain Stimulation Implants Returns Home.
15. Alhourani A, McDowell MM, Randazzo MJ, Wozny TA, Kondylis ED, et al. (2015) Network effects of deep brain stimulation. J Neurophysiol 114: 2105-2117.
16. Medtronic (2017) Medtronic SureTune(TM)3 Earns CE Mark for Deep Brain Stimulation Therapy.
17. Gorgulho A, De Salles AA, Frighetto L, Behnke E (2005) Incidence of hemorrhage associated with electrophysiological studies performed using macroelectrodes and microelectrodes in functional neurosurgery. J Neurosurg 102: 888-896.
18. Lega BC, Halpern CH, Jaggi JL, Baltuch GH (2010) Deep brain stimulation in the treatment of refractory epilepsy: update on current data and future directions. Neurobiol Dis 38: 354–360.
19. Okun M S, Zeilman P R. Deep Brain Stimulation: Practical Guide for Patients and Families.

20. Alonso F, Vogel D, Johansson J, Wårdell K, Hemm S (2018) Electric field comparison between microelectrode recording and deep brain stimulation systems—a simulation study. Brain Sci 8: 28.
21. Grill WM (2005) Safety considerations for deep brain stimulation: review and analysis. Expert Rev Med Devices 2: 409-420.
22. IEC (2015) IEC 60601-2-33:2010/COR:2016 Medical electrical equipment.
23. Medtronic (2020) MRI guidelines for Medtronic deep brain stimulation systems.
24. Boston Scientific (2017) ImageReady MRI Guidelines for Boston Scientific Deep Brain Stimulation System.
25. St. Jude Medical (2018) MRI procedure information for St. Jude Medical MR conditional deep brain stimulation system.
26. Marks Jr W J (2015) Deep brain stimulation management: Cambridge University Press.
27. Trottenberg T, Volkmann J, Deuschl G, Kühn A, Schneider G-H, et al. (2005) Treatment of severe tardive dystonia with pallidal deep brain stimulation. Neurology 64: 344-346.
28. Sako W, Goto S, Shimazu H, Murase N, Matsuzaki K, et al. (2008) Bilateral deep brain stimulation of the globus pallidus internus in tardive dystonia. Mov Disord 23: 1929-1931.
29. Cho ZH, Min HK, Oh SH, Han JY, Park CW, et al. (2010) Direct visualization of deep brain stimulation targets in Parkinson disease with the use of 7-tesla magnetic resonance imaging. J Neurosurg 113: 639-647.
30. Erhardt JB, Fuhrer E, Gruschke OG, Leupold J, Wapler MC (2018) Should patients with brain implants undergo MRI? J Neural Eng 15: 041002.
31. Finelli DA, Rezai AR, Ruggieri PM, Tkach JA, Nyenhuis JA, et al. (2002) MR imaging-related heating of deep brain stimulation electrodes: in vitro study. AJNR Am J Neuroradiol 23: 1795-802.
32. Shrivastava D, Abosch A, Hanson T, Tian J, Gupte A, et al. (2010) Effect of the extracranial deep brain stimulation lead on radiofrequency heating at 9.4 Tesla (400.2 MHz). J Magn Reson Imaging 32: 600-607.
33. Gray RW, Bibens WT, Shellock FG (2005) Simple design changes to wires to substantially reduce MRIinduced heating at 1.5 T: implications for implanted leads. Magn Reson Imaging 23: 887-891.
34. Park S, Kamondetdacha R, Amjad A, Nyenhuis J (2005) MRI safety: RF-induced heating near straight wires. IEEE Trans Magn 41: 4197-4199.
35. Nordbeck P, Fidler F, Weiss I, Warmuth M, Friedrich MT, et al. (2008) Spatial distribution of RF-induced E-fields and implant heating in MRI. Magn Reson Med 60: 312-319
36. Sammet CL, Yang X, Wassenaar PA, Bourekas EC, Yuh BA, et al. (2013) RF-related heating assessment of extracranial neurosurgical implants at 7 T. Magn Reson Imaging 31: 1029-1034.
37. Li D, Zheng J, Liu Y, Pan C, Kainz W, et al. (2015) An efficient approach to estimate MRI RF field induced in vivo heating for small medical implants. IEEE Trans Electromagn Compat 57: 643-650.
38. Cabot E, Lloyd T, Christ A, Kainz W, Douglas M, et al. (2013) Evaluation of the RF heating of a generic deep brain stimulator exposed in 1.5 T magnetic resonance scanners. Bioelectromagnetics 34: 104-113.
39. Gleason CA, Kaula NF, Hricak H, Schmidt RA, Tanagho EA (1992) The effect of magnetic resonance imagers on implanted neurostimulators. Pacing Clin Electrophysiol 15: 81-94.
40. Rezai AR, Finelli D, Nyenhuis JA, Hrdlicka G, Tkach J, et al. (2002) Neurostimulation systems for deep brain stimulation: in vitro evaluation of magnetic resonance imaging-related heating at 1.5 tesla. J Magn Reson Imaging 15: 241-250.
41. Bhusal B, Nguyen BT, Sanpitak PP, Vu J, Elahi B, et al. (2021) Effect of Device Configuration and Patient's Body Composition on the RF Heating and Nonsusceptibility Artifact of Deep Brain Stimulation Implants During MRI at 1.5T and 3T. J Magn Reson Imaging 53: 599-610.

42. Winter L, Seifert F, Zilberti L, Murbach M, Ittermann B (2020) MRI-related heating of implants and devices: a review. J Magn Reson Imaging 53: 1646-1665.
43. Brink JS (2019) Thermal effects associated with rf exposures in diagnostic mri: overview of existing and emerging concepts of protection. Conc Mag Reson P.B, Mag Reson Eng 2019.
44. Kim MS (2016) Investigation of factors affecting body temperature changes during routine clinical head magnetic resonance imaging. Iran J Radiol 13: e34016.
45. Kahan J, Papadaki A, White M, Mancini L, Yousry T, et al. (2015) The safety of using body-transmit mri in patients with implanted deep brain stimulation devices. PLoS ONE 10: e0129077.
46. Golestanirad L, Kirsch J, Bonmassar G, Downs S, Elahi B, et al. (2019) RF-induced heating in tissue near bilateral DBS implants during MRI at 1.5 T and 3T: The role of surgical lead management. Neuroimage 184: 566-576.
47. Sarkar SN, Papavassiliou E, Rojas R, Teich DL, Hackney DB, et al. (2014) Low-power inversion recovery MRI preserves brain tissue contrast for patients with parkinson disease with deep brain stimulators. AJNR Am J Neuroradiol 35: 1325-1329.
48. Mattei E, Triventi M, Calcagnini G, Censi F, Kainz W, et al. (2008) Complexity of MRI induced heating on metallic leads: Experimental measurements of 374 configurations. Biomed Eng Online 7: 11.
49. Helfer JL, Gray RW, MacDonald SG, Bibens TW (2006) Can pacemakers, neurostimulators, leads, or guide wires be MRI safe? Technological concerns and possible resolutions. Minim Invasive Ther Allied Technol 15: 114-120.
50. Panych LP, Madore B (2018) The physics of MRI safety. J Magn Reson Imaging 47: 28-43.
51. Rossi U (2003) The history of electrical stimulation of the nervous system for the control of pain. Elect Stim and the Relief of Pain, editor BA Simpson. Elsevier, Amsterdam pp: 5-16.
52. Kellaway P (1946) The part played by the electrical fish in the early history of bioelectricity and electrotherapy. Bull Hist Med 20: 112-137.
53. Schwalb JM, Hamani C (2008) The history and future of deep brain stimulation. Neurotherapeutics 5: 3-13.
54. Boling W, Olivier A, Fabinyi G (2002) Historical contributions to the modern understanding of function in the central area. Neurosurgery 50: 1296-1309, discussion 1309-1310.
55. Parent A (2004) Giovanni Aldini: from animal electricity to human brain stimulation. Can J Neurol Sci 31: 576-584.
56. Yates D (2009) Ablative surgery for Parkinson disease. Nat Rev Neurology 5: 238.
57. Sem-Jacobsen CW (1965) Depth electrographic stimulation and treatment of patients with Parkinson's disease including neurosurgical technique. Acta Neurol Scand Suppl 13 Pt 1: 365-377.
58. Dodge HW, Bickford RG, Bailey AA, Holman CB, Petersen MC, et al. (1954) Technics and Potentialities of Intracranial Electrography. Postgrad Med 15: 291-300.
59. Sem-Jacobsen CW (1966) Depth-electrographic observations related to Parkinson's disease. Recording and electrical stimulation in the area around the third ventricle. J Neurosurg 24: Suppl:388-402.
60. Blomstedt P, Hariz MI (2010) Deep brain stimulation for movement disorders before DBS for movement disorders. Parkinsonism Relat Disord 16: 429-433.
61. Choo XY, Alukaidey L, White AR, Grubman A (2013) Neuroinflammation and copper in Alzheimer's disease. Int J Alzheimers Dis 2013: 145345.
62. Dymond AM, Kaechele LE, Jurist JM, Crandall PH (1970) Brain tissue reaction to some chronically implanted metals. J Neurosurg 33: 574-580.

63. Coffey RJ (2009) Deep brain stimulation devices: a brief technical history and review. Artif Organs 33: 208-220.
64. News Release_St. Jude Medical Receives CE Mark Approval for World's Smallest, Longest-Lasting Rechargeable Deep Brain Stimulator for Parkinson's Disease.
65. CE Mark approval of the Vercise™ Deep Brain Stimulation (DBS) System for the treatment of Parkinson's disease, entering a new therapeutic category.
66. Hariz M (2014) Deep brain stimulation: new techniques. Parkinsonism Relat Disord 20 Suppl 1: S192-S196.
67. Anderson DN, Osting B, Vorwerk J, Dorval AD, Butson CR (2018) Optimized programming algorithm for cylindrical and directional deep brain stimulation electrodes. J Neural Eng 15: 026005.
68. Buhlmann J, Hofmann L, Tass PA, Hauptmann C (2011) Modeling of a segmented electrode for desynchronizing deep brain stimulation. Front Neuroeng 4: 15.
69. Willsie AC, Dorval AD (2015) Computational Field Shaping for Deep Brain Stimulation With Thousands of Contacts in a Novel Electrode Geometry. Neuromodulation 18: 542-550; discussion 550-551.
70. Park JH, Chung SJ, Lee CS, Jeon SR (2011) Analysis of hemorrhagic risk factors during deep brain stimulation surgery for movement disorders: comparison of the circumferential paired and multiple electrode insertion methods. Acta Neurochir (Wien) 153: 1573-1578.
71. Voges J, Waerzeggers Y, Maarouf M, Lehrke R, Koulousakis A, et al. (2006) Deep-brain stimulation: long-term analysis of complications caused by hardware and surgery--experiences from a single centre. J Neurol Neurosurg Psychiatry 77: 868-872.
72. Bain P G (2009) Deep Brain Stimulation. Oxford University Press.
73. Martin AJ, Larson PS, Ostrem JL, Keith Sootsman W, Talke P, et al. (2005) Placement of deep brain stimulator electrodes using real-time high-field interventional magnetic resonance imaging. Magn Reson Med 54: 1107-1114.
74. Martin AJ, Larson PS, Ostrem JL, Starr PA (2009) Interventional magnetic resonance guidance of deep brain stimulator implantation for Parkinson disease. Top Magn Reson Imaging 19: 213-221.
75. Starr PA, Markun LC, Larson PS, Volz MM, Martin AJ, et al. (2014) Interventional MRI-guided deep brain stimulation in pediatric dystonia: first experience with the ClearPoint system. J Neurosurg Pediatr 14: 400-408.
76. Falowski S, Safriel Y, Ryan MP, Hargens L (2016) The Rate of Magnetic Resonance Imaging in Patients with Deep Brain Stimulation. Stereotact Funct Neurosurg 94: 147-153.
77. Chandran AS, Bynevelt M, Lind CR (2016) Magnetic resonance imaging of the subthalamic nucleus for deep brain stimulation. J Neurosurg 124: 96-105.
78. Saenger VM, Kahan J, Foltynie T, Friston K, Aziz TZ, et al. (2017) Uncovering the underlying mechanisms and whole-brain dynamics of deep brain stimulation for Parkinson's disease. Sci Rep 7: 9882.
79. Kahan J, Mancini L, Urner M, Friston K, Hariz M, et al. (2012) Therapeutic subthalamic nucleus deep brain stimulation reverses cortico-thalamic coupling during voluntary movements in Parkinson's disease. PLoS One 7: e50270.
80. Min HK, Ross EK, Lee KH, Dennis K, Han SR, et al. (2014) Subthalamic nucleus deep brain stimulation induces motor network BOLD activation: use of a high precision MRI guided stereotactic system for nonhuman primates. Brain Stimul 7: 603-607.
81. Tang CC, Eidelberg D (2013) Brain stimulation and functional imaging with fMRI and PET. Handb Clin Neurol 116: 77-95.

82. Sweet JA, Walter BL, Gunalan K, Chaturvedi A, McIntyre CC, et al. (2014) Fiber tractography of the axonal pathways linking the basal ganglia and cerebellum in Parkinson disease: implications for targeting in deep brain stimulation. J Neurosurg 120: 988-996.
83. Riva-Posse P, Choi KS, Holtzheimer PE, McIntyre CC, Gross RE, et al. (2014) Defining critical white matter pathways mediating successful subcallosal cingulate deep brain stimulation for treatment-resistant depression. Biol Psychiatry 76: 963-969.
84. Kovanlikaya I, Heier L, Kaplitt M (2014) Treatment of chronic pain: diffusion tensor imaging identification of the ventroposterolateral nucleus confirmed with successful deep brain stimulation. Stereotact Funct Neurosurg 92: 365-371.
85. Reich CA, Hudgins PA, Sheppard SK, Starr PA, Bakay RA (2000) A high-resolution fast spin-echo inversion-recovery sequence for preoperative localization of the internal globus pallidus. AJNR Am J Neuroradiol 21: 928-931.
86. Cheng CH, Huang HM, Lin HL, Chiou SM (2014) 1.5T versus 3T MRI for targeting subthalamic nucleus for deep brain stimulation. Br J Neurosurg 28: 467-470.
87. Kandel ER, Schwartz JH, Jessell TM, Siegelbaum SA, Hudspeth AJ (2000) Principles of neural science. (5th edn.) McGraw-hill, New York.
88. Tourdias T, Saranathan M, Levesque IR, Su J, Rutt BK (2014) Visualization of intra-thalamic nuclei with optimized white-matter-nulled MPRAGE at 7T. Neuroimage 84: 534-545.
89. Lemaire JJ, Sakka L, Ouchchane L, Caire F, Gabrillargues J, et al. (2010) Anatomy of the human thalamus based on spontaneous contrast and microscopic voxels in high-field magnetic resonance imaging. Neurosurgery 66(3 Suppl Operative): 161-172.
90. Abosch A, Yacoub E, Ugurbil K, Harel N (2010) An assessment of current brain targets for deep brain stimulation surgery with susceptibility-weighted imaging at 7 tesla. Neurosurgery 67: 1745-1756; discussion 1756.
91. Deistung A, Schäfer A, Schweser F, Biedermann U, Turner R, et al. (2013) Toward in vivo histology: a comparison of quantitative susceptibility mapping (QSM) with magnitude-, phase-, and R2*-imaging at ultra-high magnetic field strength. Neuroimage 65: 299-314.
92. Behrens TE, Johansen-Berg H, Woolrich MW, Smith SM, Wheeler-Kingshott CA, et al. (2003) Non-invasive mapping of connections between human thalamus and cortex using diffusion imaging. Nat Neurosci 6: 750-757.
93. Deoni SC, Rutt BK, Parrent AG, Peters TM (2007) Segmentation of thalamic nuclei using a modified k-means clustering algorithm and high-resolution quantitative magnetic resonance imaging at 1.5 T. Neuroimage 34: 117-126.
94. Vassal F, Coste J, Derost P, Mendes V, Gabrillargues J, et al. (2012) Direct stereotactic targeting of the ventrointermediate nucleus of the thalamus based on anatomic 1.5-T MRI mapping with a white matter attenuated inversion recovery (WAIR) sequence. Brain Stimul 5: 625-633.
95. Zerroug A, Gabrillargues J, Coll G, Vassal F, Jean B, et al. (2016) Personalized mapping of the deep brain with a white matter attenuated inversion recovery (WAIR) sequence at 1.5-tesla: Experience based on a series of 156 patients. Neurochirurgie 62: 183-189.
96. Henderson JM, Tkach J, Phillips M, Baker K, Shellock FG, et al. (2005) Permanent neurological deficit related to magnetic resonance imaging in a patient with implanted deep brain stimulation electrodes for Parkinson's disease: case report. Neurosurgery 57: E1063; discussion E1063.

97. Boutet A, Rashid T, Hancu I, Elias GJB, Gramer RM, et al. (2019) Functional MRI Safety and Artifacts during Deep Brain Stimulation: Experience in 102 Patients. Radiology 293: 174-183.
98. Phillips MD, Baker KB, Lowe MJ, Tkach JA, Cooper SE, et al. (2006) Parkinson disease: pattern of functional MR imaging activation during deep brain stimulation of subthalamic nucleus--initial experience. Radiology 239: 209-216.
99. Sammartino F, Krishna V, Sankar T, Fisico J, Kalia SK, et al. (2017) 3-Tesla MRI in patients with fully implanted deep brain stimulation devices: a preliminary study in 10 patients. J Neurosurg 127: 892-898.
100. Zrinzo L, Yoshida F, Hariz MI, Thornton J, Foltynie T, et al. (2011) Clinical safety of brain magnetic resonance imaging with implanted deep brain stimulation hardware: large case series and review of the literature. World Neurosurg 76: 164-72; discussion 69-73.
101. Englot DJ, Glastonbury CM, Larson PS (2011) Abnormal T2-weighted MRI signal surrounding leads in a subset of deep brain stimulation patients. Stereotact Funct Neurosurg 89: 311-317.
102. Zekaj E, Saleh C, Menghetti C, Servello D (2013) Does magnetic resonance imaging induce tissue damage due to DBS lead heating? Acta Neurochir (Wien) 155: 1677-1678.
103. Lefaucheur R, Derrey S, Borden A, Wallon D, Ozkul O, et al. (2013) Post-operative edema surrounding the electrode: an unusual complication of deep brain stimulation. Brain Stimul 6: 459-460.
104. Deogaonkar M, Nazzaro JM, Machado A, Rezai A (2011) Transient, symptomatic, post-operative, non-infectious hypodensity around the deep brain stimulation (DBS) electrode. J Clin Neurosci 18: 910-915.
105. Georgi JC, Stippich C, Tronnier VM, Heiland S (2004) Active deep brain stimulation during MRI: a feasibility study. Magn Reson Med 51: 380-388.
106. Boutet A, Hancu I, Saha U, Crawley A, Xu DS, et al. (2019) 3-Tesla MRI of deep brain stimulation patients: safety assessment of coils and pulse sequences. J Neurosurg 132: 586-594.
107. Eryaman Y, Lagore RL, Ertürk MA, Utecht L, Zhang P, et al. (2018) Radiofrequency heating studies on anesthetized swine using fractionated dipole antennas at 10.5 T. Magn Reson Med 79: 479-488.
108. Bottomley PA (2008) Turning up the heat on MRI. J Am Coll Radiol. 5: 853-855.
109. Baker KB, Tkach JA, Nyenhuis JA, Phillips M, Shellock FG, et al. (2004) Evaluation of specific absorption rate as a dosimeter of MRI-related implant heating. J Magn Reson Imaging 20: 315-320.
110. Shrivastava D, Hanson T, Schlentz R, Gallaghar W, Snyder C, et al. (2008) Radiofrequency heating at 9.4T: in vivo temperature measurement results in swine. Magn Reson Med 59: 73-78.
111. McElcheran CE, Golestanirad L, Iacono MI, Wei PS, Yang B, et al. (2019) Numerical Simulations of Realistic Lead Trajectories and an Experimental Verification Support the Efficacy of Parallel Radiofrequency Transmission to Reduce Heating of Deep Brain Stimulation Implants during MRI. Sci Rep 9: 2124.
112. Iacono MI, Makris N, Mainardi L, Angelone LM, Bonmassar G (2013) MRI-Based Multiscale Model for Electromagnetic Analysis in the Human Head with Implanted DBS. Comput Math Methods Med 2013: 694171.
113. Angelone LM, Ahveninen J, Belliveau JW, Bonmassar G (2010) Analysis of the role of lead resistivity in specific absorption rate for deep brain stimulator leads at 3T MRI. IEEE Trans Med Imaging 29: 1029-1038.
114. Guerin B, Serano P, Iacono MI, Herrington TM, Widge AS, et al. (2018) Realistic modeling of deep brain stimulation implants for electromagnetic MRI safety studies. Phys Med Biol 63: 095015.
115. Yao A, Zastrow E, Neufeld E, Kuster N (2019) Efficient and Reliable Assessment of the Maximum Local Tissue Temperature Increase at the Electrodes of Medical Implants under MRI Exposure. Bioelectromagnetics 40: 422-433.

116. Eichfelder G, Gebhardt M (2011) Local specific absorption rate control for parallel transmission by virtual observation points. Magn Reson Med 66: 1468-1476.
117. Winkler SA, Saniour I, Chaudhari A, Robb F, Vaughan JT (2020) MRSaiFE: Tissue Heating Prediction for MRI: A Feasibility Study. 2020 IEEE MTT-S International Microwave Biomedical Conference (IMBioC): 1-3.
118. Van Rhoon GC, Samaras T, Yarmolenko PS, Dewhirst MW, Neufeld E, et al. (2013) CEM43°C thermal dose thresholds: A potential guide for magnetic resonance radiofrequency exposure levels? Eur Radiol 23: 2215-2227.
119. Sapareto SA, Dewey WC (1984) Thermal dose determination in cancer therapy. Int J Radiat Oncol Biol Phys 10: 787-800.
120. Yarmolenko PS, Moon EJ, Landon C, Manzoor A, Hochman DW, et al. (2011) Thresholds for thermal damage to normal tissues: an update. Int J Hyperthermia 27: 320-343.
121. Pennes HH (1948) Analysis of tissue and arterial blood temperatures in the resting human forearm. Appl Physiol 1: 93-122.
122. Kotte A, van Leeuwen G, de Bree J, van der Koijk J, Crezee H, et al. (1996) A description of discrete vessel segments in thermal modelling of tissues. Phys Med Biol 41: 865-884.
123. Collins CM, Liu W, Wang J, Gruetter R, Vaughan JT, et al. (2004) Temperature and SAR Calculations for a Human Head Within Volume and Surface Coils at 64 and 300 MHz. J Magn Reson Imag 19: 650-656.
124. Wang Z, Lin JC, Mao W, Liu W, Smith MB, et al. (2007) SAR and temperature: simulations and comparison to regulatory limits for MRI. J Magn Reson Imaging 26: 437-441.
125. National Council on Radiation Protection and Measurements (1986) Biological effects and exposure criteria for radiofrequency electromagnetic fields. Report No. 86. Bethesda, MD.
126. Gordon CJ (1984) Thermal physiology. In: Biological effects of radiofrequency radiation. Washington, DC: EPA-600/8-83-026A: 4-1–4-28.
127. Gordon CJ (1988) Effect of radiofrequency radiation exposure on thermoregulation. ISI Atlas Sci Plants Anim 1: 245-250.
128. Michaelson SM, Lin JC (1987) Biological effects and health implications of radiofrequency radiation. Springer, Boston.
129. McElcheran CE, Yang B, Anderson KJT, Golestanirad L, Graham SJ (2017) Parallel radiofrequency transmission at 3 tesla to improve safety in bilateral implanted wires in a heterogeneous model. Magn Reson Med 78: 2406-2415.
130. Del Bene VE (1990) Temperature (Ch 218). Walker HK, Hall WD, Hurst JW, editors. In: Clinical Methods: The History, Physical, and Laboratory Examinations, Boston (Butterworths) pp:990-993.
131. Wang H, Wang B, Normoyle KP, Jackson K, Spitler K, et al. (2014) Brain temperature and its fundamental properties: A review for clinical neuroscientists. Front Neurosci 8: 307.
132. Shellock FG, Crues JV (2004) MR procedures: biologic effects, safety, and patient care. Radiol 232: 635-652.
133. Davidson B, Elkaim LM, Lipsman N, Ibrahim GM (2018) An ethical framework for deep brain stimulation in children. Neurosurg Focus 45: E11.
134. Dempsey MF, Condon B, Hadley DM (2001) Investigation of the factors responsible for burns during MRI. J Magn Reson Imaging 13: 627-631.
135. Zheng J, Xia M, Kainz W, Chen J (2020) Wire-based sternal closure: MRI-related heating at 1.5 T/64 MHz and 3 T/128 MHz based on simulation and experimental phantom study. Magn Reson Med 83: 1055-1065.

136. Keil B, Blau JN, Biber S, Hoecht P, Tountcheva V, et al. (2013) A 64-channel 3T array coil for accelerated brain MRI. Magnetic resonance in medicine 70: 248-258.
137. Pruessmann KP, Weiger M, Scheidegger MB, Boesiger P (1999) SENSE: sensitivity encoding for fast MRI. Magn Reson Med 42: 952-962.
138. Griswold MA, Jakob PM, Heidemann RM, Nittka M, Jellus V, et al. (2002) Generalized autocalibrating partially parallel acquisitions (GRAPPA). Magn Reson Med 47: 1202-1210.
139. Baker KB, Tkach J, Hall JD, Nyenhuis JA, Shellock FG, et al. (2005) Reduction of magnetic resonance imaging-related heating in deep brain stimulation leads using a lead management device. Neurosurgery 57: 392-397.
140. Golestanirad L, Angelone LM, Ida Iacono M, Katnani H, Wald LL, et al. (2017) Local SAR near deep brain stimulation (DBS) electrodes at 64 and 127 MHz: A simulation study of the effect of extracranial loops. Magn Reson Med 78: 1558-1565.
141. Sree Harsha NR, Prakash A, Kothari DP (2016) The foundations of electric circuit theory, 2053-2563, IOP Publishing.
142. Ranck Jr JB (1975) Which elements are excited in electrical stimulation of mammalian central nervous system: a review. Brain Res 98: 417-440.
143. Hashimoto T, Elder CM, Okun MS, Patrick SK, Vitek JL (2003) Stimulation of the subthalamic nucleus changes the firing pattern of pallidal neurons. J Neurosci 23: 1916-1923.
144. Davidson B, Tam F, Yang B, Meng Y, Hamani C, et al. (2021) Three-Tesla Magnetic Resonance Imaging of Patients With Deep Brain Stimulators: Results From a Phantom Study and a Pilot Study in Patients. Neurosurgery 88: 349-355.
145. Etezadi-Amoli M, Stang P, Kerr A, Pauly J, Scott G (2015) Controlling radiofrequency-induced currents in guidewires using parallel transmit. Magn Reson Med 74: 1790-1802.
146. Guerin B, Angelone LM, Dougherty D, Wald LL (2020) Parallel transmission to reduce absorbed power around deep brain stimulation devices in MRI: Impact of number and arrangement of transmit channels. Magn Reson Med 83: 299-311.
147. Eryaman Y, Guerin B, Akgun C, Herraiz JL, Martin A, et al. (2015) Parallel transmit pulse design for patients with deep brain stimulation implants. Magn Reson Med 73: 1896-1903.
148. Seifert F, Weidemann G, Ittermann B (2015) Q matrix approach to control implant heating by transmit array coils. Proc Intl Soc Mag Reson Med 23: 3212.
149. Godinez F, Scott G, Padormo F, Hajnal JV, Malik SJ (2020) Safe guidewire visualization using the modes of a PTx transmit array MR system. Magn Reson Med 83: 2343-2355.
150. Destruel A, Fuentes M, Weber E, O'Brien K, Jin J, et al. (2019) A numerical and experimental study of RF shimming in the presence of hip prostheses using adaptive SAR at 3T. Magn Reson Med 81: 3826-3839.
151. Winter L, Silemek B, Petzold J, Pfeiffer H, Hoffmann W, et al. (2020) Parallel transmission (pTx) medical implant safety testbed: real-time mitigation of RF induced tip heating using timedomain E-field sensors. Magn Reson Med 84: 3468-3484.
152. Eryaman Y, Akin B, Atalar E (2011) Reduction of implant RF heating through modification of transmit coil electric field. Magn Reson Med 65: 1305-1313.
153. Golestanirad L, Keil B, Angelone LM, Bonmassar G, Mareyam A, et al. (2017) Feasibility of using linearly polarized rotating birdcage transmitters and close-fitting receive arrays in MRI to reduce SAR in the vicinity of deep brain simulation implants. Magn Reson Med 77: 1701-1712.

154. Schenck JF (1996) The role of magnetic susceptibility in magnetic resonance imaging: MRI magnetic compatibility of the first and second kinds. Med Phys 23: 815-850.
155. Zhao S, Li G, Tong C, Chen W, Wang P, et al. (2020) Full activation pattern mapping by simultaneous deep brain stimulation and fMRI with graphene fiber electrodes. Nat Commun 11: 1788.
156. Pollo C, Villemure J-G, Vingerhoets F, Ghika J, Maeder P, et al. (2004) Magnetic resonance artifact induced by the electrode Activa 3389: an in vitro and in vivo study. Acta Neurochir 146: 161-164.
157. Bodart C, Rossetti N, Hagler J, Chevreau P, Chhin D, et al. (2019) Electropolymerized Poly(3,4-ethylenedioxythiophene) (PEDOT) Coatings for Implantable Deep-Brain-Stimulating Microelectrodes. ACS Appl Mater Interfaces 11: 17226-17233.
158. Green RA, Lovell NH, Wallace GG, Poole-Warren LA (2008) Conducting polymers for neural interfaces: challenges in developing an effective long-term implant. Biomaterials 29: 3393-3399.
159. Cui XT, Zhou DD (2007) Poly (3,4-ethylenedioxythiophene) for chronic neural stimulation. IEEE Trans Neural Syst Rehabil Eng 15: 502-508.
160. Martínez-Santiesteban FM, Scott DS, Douglas CN, David JA (2006) Magnetic resonance compatibility of multichannel silicon microelectrode systems for neural recording and stimulation: design criteria, tests, and recommendations. IEEE Trans Biomed Eng 53: 547-558.
161. Beygi M, Dominguez-Viqueira W, Feng C, Mumcu G, Frewin CL, et al. (2021) Silicon Carbide and MRI: Towards Developing a MRI Safe Neural Interface. Micromachines (Basel) 12: 126.
162. Bonmassar G, Fujimoto K, Golby AJ (2012) PTFOS:flexible and absorbable intracranial electrodes for magnetic resonance imaging. PLoS ONE 7: e41187.
163. Yoon H, Deshpande DC, Kim TH, Jeong EK, Harbaugh RE, et al. (2010) Development of titanium needle probes for neural recording and evaluation of magnetic resonance imaging artifacts. J Nanotechnol Eng Med 1: 011004.
164. Jiang CQ, Hao HW, Li LM (2013) Artifact properties of carbon nanotube yarn electrode in magnetic resonance imaging. J Neural Eng 10: 026013.
165. Seeber DA, Jevtic J, Menon A (2004) Floating shield current suppression trap. Concepts Magn Reson B (Magn Reson Eng) 21B: 26-31.
166. Griffin GH, Anderson KJT, Wright GA (2017) Miniaturizing floating traps to increase RF safety of magnetic-resonance-guided percutaneous procedures. IEEE Trans Biomed Eng 64: 329-340.
167. Alipour A, Meyer ES, Dumoulin CL, Watkins RD, Elahi H, et al. (2020) MRI Conditional Actively Tracked Metallic Electrophysiology Catheters and Guidewires With Miniature Tethered Radio-Frequency Traps: Theory, Design, and Validation. IEEE Trans Biomed Eng 67: 1616-1627.
168. Reilly JP (1998) Applied bioelectricity: from electrical stimulation to electropathology. New York: Springer Verlag pp: 412.
169. Bonmassar G (2004) Resistive tapered stripline (RTS) in electroencephalogram recordings during MRI. IEEE Trans Microw Theory Tech 52: 1992-1998.
170. Ladd ME, Quick HH (2000) Reduction of resonant RF heating in intravascular catheters using coaxial chokes. Magn Reson Med 43: 615-619.
171. Shaw RK, Long B, Werner D, Gavrin A (2007) The characterization of conductive textile materials intended for radio frequency applications. IEEE Antennas Propag Mag 49: 28-40.